Transport in Porous Media (2026) 153:63
https://doi.org/10.1007/s11242-026-02315-3

Coupled Dissolution and Diffusive Interactions of Microbubbles in Irregular Pore Networks

Nerine Joewondo[1] · Valeria Garbin[1,2] · Ronny Pini[1]

Received: 8 December 2025 / Accepted: 24 April 2026

Abstract

The dissolution of a dispersed gas phase in a porous medium partially saturated with liquid is a problem of broad practical interest. While capillary equilibration has been shown to affect the evolution of the dispersed phase, its coupling with the underlying diffusive process in the liquid phase remains largely unexplored. Here, we deploy a pore-network model to describe coupled dissolution and diffusive interactions of a lattice of microbubbles in irregular pore networks. We demonstrate that the dissolution process becomes more erratic than in regular networks, because of the complex interplay between local connectivity effects and diffusive shielding between neighboring bubbles. By applying the method of moments, we quantify the evolution of solute mass in the system and compute continuum-scale properties, such as the effective diffusion coefficient of the network and the dissolution rate of the bubble lattice. We observe that the presence of bubbles delays the attainment of an asymptotic diffusive behavior and reduces the spatial extent of the solute plume relative to the same liquid-saturated network. Importantly, collective effects appear to be stronger than effects associated with the local pore connectivity distribution in the network in reducing the rate of dissolution of bubbles.

Article Highlights

- Local connectivity and collective effects control the dissolution of microbubbles in irregular pore networks
- Bubbles can grow significantly before undergoing complete dissolution
- The presence of bubbles delays the dissolution process and reduces the spatial extent of the solute plume relative to a bubble-free network
- The complex topology of practical porous media may strengthen collective effects even further

Keywords Bubble dissolution · Porous media · Diffusive transport · Pore-network model

✉ Valeria Garbin
v.garbin@tudelft.nl

✉ Ronny Pini
r.pini@imperial.ac.uk

[1] Department of Chemical Engineering, Imperial College London, London SW7 2AZ, United Kingdom

[2] Department of Chemical Engineering, Delft University of Technology, 2629 HZ Delft, The Netherlands

Published online: 14 May 2026

1 Introduction

Bubbles trapped in a porous medium form a discontinuous phase that interacts with the continuous phase surrounding them through several mechanisms, including diffusion and capillarity (Adam et al. 1969). The study of the evolution of this dispersed phase underpins applications in both traditional and emerging engineering problems that occur in natural environments. Entrapped air bubbles in the vadose zone play a major role for the gas exchange between the atmosphere and groundwater (Holocher et al. 2003), and represent a source of oxygen for aerobic in situ bioremediation of contaminants in soil (Fry et al. 1997). The long-term storage of carbon dioxide (CO_2) in subsurface saline aquifers relies on the efficacy of capillary trapping—the immobilization of CO_2 in the pore space of the rock as disconnected ganglia Krevor et al. (2015)—and the subsequent dissolution of this dispersed gas phase in the surrounding brine (Patmonoaji and Suekane 2017). Yet, the diffusive transport of dissolved gas in the continuous aqueous phase may lead to the redistribution of the ganglia to reach local capillary equilibrium Moghadasi et al. (2023)—a phenomenon referred to as Ostwald ripening (Schmelzer and Schweitzer 1987). In addition to CO_2 (Chalendar et al. 2018; Li et al. 2020), the latter bears potential implications for the subsurface storage of other gases, including hydrogen, methane and nitrogen (Blunt 2022).

In the case of dissolving bubbles in a stagnant liquid phase, the key driving physical mechanisms are the dissolution of the gas into the liquid to maintain equilibrium at the gas–liquid interface, and the transport of the dissolved gas within the liquid phase (Epstein and Plesset 1950). The inherent disorder of natural porous media, such as rocks or soil, challenges the quantitative description of these processes. The tortuosity of the pore space limits transport fluxes in the continuous liquid phase (Shen and Chen 2007), generating solute concentration fields that are complex and difficult to predict, both in the presence (Dentz et al. 2011) and absence of flow (Sadeghi et al. 2017). The disconnected gas phase acts here as an additional effective disperser by increasing the tortuosity of the flow paths, yielding enhanced mixing rates (Jiménez-Martínez et al. 2015). The texture of the porous medium determines the capillary pressure of the trapped gas phase and, accordingly, dissolution kinetics at discrete gas–liquid interfaces (Adam et al. 1969). The amount and distribution of the gas phase in the pore space dictates the resultant mass exchange process; in fact, each bubble in the system may act as a source, releasing gas into the liquid phase, or a sink, uptaking gas from the liquid phase, thus affecting locally the liquid saturation and the dissolution (or growth) of neighboring bubbles (Xu et al. 2017; Mehmani and Xu 2022; Yu et al. 2023). Studies investigating the role of such collective effects on the diffusion of dissolved gas *within* the liquid phase are just beginning (Michelin et al. 2018), and remain largely unexplored for porous systems (Joewondo et al. 2022; Turkoz et al. 2023).

Coupled dissolution and diffusion of a nonwetting phase in porous media have been modeled at different length scales. Continuum models (e.g., Powers et al. (1991); Holocher et al. (2003)), which are based on an effective interphase mass transfer coefficient, can predict the system's behavior using volume-averaged variables, such as the concentration of solute and the saturation of each phase. In pore-network modeling (PNM, e.g., Dillard and Blunt (2000)), both the actual location of fluid–fluid interfaces and the pore-network topology are explicitly taken into account, and processes in the network are described using fundamental physical laws. By enabling the integration of events in an interacting ensemble of pores, this approach also offers the opportunity to carry out upscaling from physical observations at representative length scales Held and Celia (2001)—informing the continuum-scale models described above. These early works on coupled dissolution and diffusion studied liquid–

liquid systems, in the context of the dissolution of a non-aqueous liquid dispersed in an aqueous phase. The use of PNM to describe the evolution of bubbles is less common, and only recently formulations have been presented that account for local interfacial curvatures and the associated Laplace pressure (Chalendar et al. 2018; Wang et al. 2021). Yet, focus in these studies has been largely placed on the resultant (equilibrium) distribution of bubbles, rather than on the evolution of the solute concentration field within the network. The latter is key to fully comprehend the interplay of dissolution *and* diffusion, which ultimately governs the fate of dispersed gas in porous media.

Here, we set out to investigate using PNM the characteristic behaviors of the collective bubble dissolution process in irregular pore networks. The latter refer to networks where the pore body connectivity varies locally. To this end, we present and apply the extension of our previous model formulation for regular and uniform pore networks (Joewondo et al. 2022). To evaluate collective effects, we quantify the temporal and spatial evolution of solute mass in the system (both in the gas and liquid phase) and apply the method of moments. We extract features of the dissolution process arising specifically from the presence of bubbles by comparing simulations with and without bubbles in the same network. The emerging pore-scale transport behavior is used to compute continuum-scale properties, such as the rate of expansion of the solute plume, the effective diffusion coefficient and the effective dissolution rate of the bubble population. We show that the latter cannot be extrapolated directly from that of an individual bubble, because it also depends on the effective dissipation rate of the dissolved solute phase.

2 Pore-Network Model

The pore-network model is an extension to irregular networks of our previous formulation for regular and uniform pore networks (Joewondo et al. 2022). The model combines two transport mechanisms characterized by distinct mass transfer rates: bubble dissolution, which couples the gas phase with the solute concentration in the liquid, and diffusive transport of solute throughout the network. The model formulation is briefly summarized here, and the reader is referred to Joewondo et al. (2022) for a detailed explanation.

2.1 Coupled Dissolution and Diffusive Transport Formulation

The key features of the pore-network model are depicted in Fig. 1. The pore network consists of P spherical pore bodies of equal radius R_p. Each pore body is connected to neighboring pore bodies by $N_{\mathrm{t},i}$ cylindrical pore throats, where the index $i = 1, ..., P$ identifies a pore in the network. All pore throats in the network are identical, with radius R_t and length L_t. Each pore body can be occupied by no more than one spherical bubble, fixed at the center of the pore, with bubble radius $R_i < R_\mathrm{p}$. Following a pore-network model approach, the concentration of dissolved gas in the liquid in pore i, $C_{\mathrm{p},i}$, is assumed to be uniform. This assumption is justified so long as the diffusive timescale is much faster than the bubble dissolution timescale, for instance, for gases with sufficiently high diffusivity (Joewondo et al. 2022), such that the concentration gradients are localized in a boundary layer near the surface of the bubble whose width is small compared to the pore radius. The only concentration gradients in the bulk liquid are then between neighboring pore bodies, i and j, as illustrated in Fig. 1.

The radius of a bubble in pore i, $R_i(t)$, evolves in time due to mass transfer of gas between the bubble and the liquid. Our description of mass transfer between a gas bubble and the

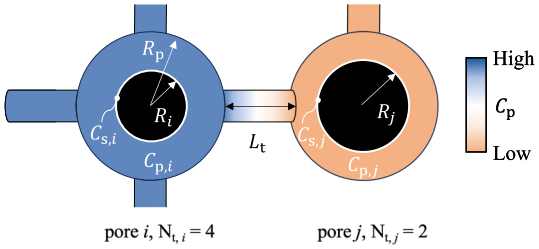

Fig. 1 Schematic of the irregular pore-network geometry. Spherical pore bodies of radius R_p are connected by cylindrical pore throats of length L_t. The connectivity of pore i, defined as the number of pore throats connecting pore i to neighboring pores, is $N_{t,i}$. A spherical gas bubble located in pore body i has radius R_i and is positioned at the center of the pore body at all times. The pore space surrounding a bubble is occupied by liquid with a uniform dissolved gas concentration $C_{p,i}$, while $C_{s,i}$ is the local saturation concentration in pore i, which depends on the bubble radius because of the effect of the Laplace pressure. The only concentration gradients in the bulk liquid are between neighboring pore bodies

surrounding liquid is based on the classical model for isolated, single-component, spherical gas bubbles in a quiescent, incompressible liquid in an unbounded domain (Epstein and Plesset 1950). To combine this description with the pore-network formulation, we simplified this model by assuming that the concentration of solute in the liquid in pore body i, $C_{p,i}$, is uniform, keeping in mind that this assumption is only justified so long as $R_i \ll R_p$. The solute concentration in the pore, $C_{p,i}$, evolves in time due to mass exchange with the bubble residing in the pore, and diffusion through the liquid to the neighboring pores. Gas will diffuse into or out of the bubble, depending on whether $C_{p,i} < C_{s,i}$ or $C_{p,i} > C_{s,i}$, until the equilibrium or saturation concentration of dissolved gas in pore i, $C_{s,i}$, is reached. The latter depends on the partial pressure of gas in contact with the liquid *via* Henry's law: $C_{s,i} = k_H M P_{b,i}$, where k_H [mol/(Pa m^3)] is Henry's constant, M [kg/mol] is the molar mass of the gas, and $P_{b,i}$ [Pa] is the gas pressure inside the bubble in pore i. The gas pressure in the bubble has contributions from the pressure of the liquid, P^0, and the capillary (Laplace) pressure: $P_{b,i} = P^0 + 2\gamma {R_i}^{-1}$, where γ is the surface tension of the gas–liquid interface. Therefore, the saturation concentration $C_{s,i}$ is a local property of pore i that depends on the radius of the bubble located in that pore. The pressure of the liquid, P^0, is assumed to be uniform throughout the network and constant, such that advection can be ignored.

Assuming spherical symmetry and negligible inertial effects in the liquid during motion of the bubble interface, and after an initial transient period (Epstein and Plesset 1950), the rate of change of the radius of bubble i is:

$$\frac{dR_i}{dt} = \mathcal{D}(C_{p,i} - C_{s,i})\left(\rho^0 + \frac{4M\gamma}{3R_g T R_i}\right)^{-1} \frac{1}{R_i}, \tag{1}$$

where $\mathcal{D}$ is the diffusion coefficient of the gas in the liquid. The terms in the second parenthesis account for the ideal gas density associated with the gas pressure $P_{b,i}$ inside a bubble:

$$\rho_{b,i} = \rho^0 + \frac{2\gamma}{R_i}\frac{M}{R_g T}, \tag{2}$$

where $\rho^0 = MP^0/(R_g T)$ is the ideal gas density corresponding to the gas pressure for a planar interface, equal to P^0, and with R_g the ideal gas constant and T the temperature.

The mass flux through the gas–liquid interface in pore body i is:

$$J_{i\to i} = -\frac{\mathcal{D}}{R_i}(C_{\mathrm{p},i} - C_{\mathrm{s},i}). \tag{3}$$

The sign convention implies that solute uptake by the liquid phase within pore body i is characterized by a positive value of the flux.

The mass flux between neighboring pore bodies j and i is driven by a spatial concentration gradient and is expressed by the one-dimensional form of Fick's first law:

$$J_{j\to i} = -\frac{\mathcal{D}}{L_\mathrm{t}}(C_{\mathrm{p},i} - C_{\mathrm{p},j}), \tag{4}$$

Accounting for these two diffusive processes, the temporal evolution of the solute concentration in pore body i containing a bubble of radius R_i is described by the following differential equation:

$$\begin{aligned}\frac{dC_{\mathrm{p},i}}{dt} = &-\mathcal{D}\frac{A_\mathrm{t}}{L_\mathrm{t}\epsilon_i V_\mathrm{p}}\sum_{j=1}^{N_\mathrm{t}}(C_{\mathrm{p},i} - C_{\mathrm{p},j}) \\ &-\frac{4\pi R_i^2}{\epsilon_i V_\mathrm{p}}\frac{dR_i}{dt}\left(\rho^0 + \frac{4M\gamma}{3R_\mathrm{g}TR_i} - C_{\mathrm{p},i}\right),\end{aligned} \tag{5}$$

where $V_\mathrm{p} = 4\pi R_\mathrm{p}^3/3$ is the volume of a pore body, and $\epsilon_i = 1 - V_i/V_\mathrm{p}$ is the volume fraction of liquid in the pore body, $V_i = 4\pi R_i^3/3$ being the volume of the bubble in the pore body. Together, Eqs. 1 and 5 represent the system of coupled differential equations to be solved for the two variables $C_{\mathrm{p},i}$ and R_i for each pore body in the network.

It is useful to define the degree of liquid saturation in a pore relative to the saturation concentration for a planar interface, $C_\mathrm{s}^0 = k_\mathrm{H}MP^0$:

$$f = C_{\mathrm{p},i}/C_\mathrm{s}^0. \tag{6}$$

Integration of Eq. 1 yields the dissolution time of a single isolated bubble of initial radius R^0 in a gas-saturated liquid ($f = 1$) Duncan and Needham (2004):

$$t_\mathrm{d}^* = \frac{(R^0)^2}{3\mathcal{D}k_\mathrm{H}}\left(\frac{R^0\rho^0}{2M\gamma} + \frac{1}{R_\mathrm{g}T}\right). \tag{7}$$

We will use the dissolution time t_d^* throughout this work as the reference value for an isolated bubble, to quantify the effects caused by the presence of a pore-network and by multiple bubbles. We therefore define a dimensionless time $\tau = t/t_\mathrm{d}^*$.

2.2 Numerical Implementation

For a network of P pore bodies, Eqs. 1 and 5 must be solved simultaneously for all pore bodies at each time step. To this end, the equations have been implemented using graph theory in a structured network with equally spaced pore bodies in a two-dimensional Cartesian coordinate system (in pore units, p.u.), as depicted in Fig. 2. The pore body in the center is at $\{x, y\} = \{0, 0\}$ and its immediate neighbor on the right is at $\{x, y\} = \{1, 0\}$. We considered networks with domain size $P = 171 \times 171 = 29,241$ pore bodies, where pore bodies in the outermost layer have an imposed radius $100 \times R_\mathrm{p}$ and represent—effectively—an open boundary. This domain size is sufficient to avoid boundary effects affecting the diffusive transport of the solute plume. Indeed, as discussed in Sect. 4.3 for simulations without

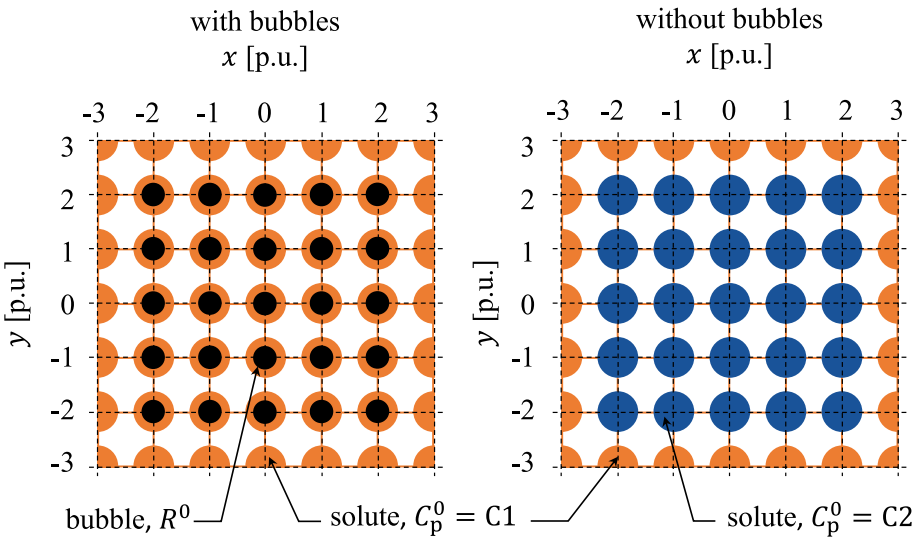

Fig. 2 Schematics of the initial setup of the simulation scenarios "with bubbles" (left) and "without bubbles" (right). In the first one, 25 bubbles ($R^0 = 1\ \mu$m) are positioned in a dense square lattice in the center of the network. The initial solute concentration, C_p^0, of all pore bodies in the system is uniform (i.e. $C_p^0 = $ C1). In the second case, dissolved solute is introduced in place of the bubbles at a concentration $C_p^0 = $ C2 $>$ C1 such that the total mass of solute is the same in both scenarios. For both scenarios, the network has 171×171 pore bodies. Only the area of the network $-3 \le x \le 3$ and $-3 \le y \le 3$ is shown here

bubbles, we confirm attainment of the so-called asymptotic regime, whereby the second central moment of the solute plume grows linearly with time (constant effective diffusion coefficient). For a given set of initial conditions, Eqs. 1 and 5 are solved using the `ode45` solver in MATLAB with a relative error tolerance `'RelTol'` $= 10^{-8}$ and absolute error tolerances on the variables R_i and $C_{p,i}$ of $10^{-4}\ \mu$m and 10^{-10} kg/m^3, respectively.

2.3 Network Connectivity

To investigate the effect of the pore-network geometry, we constructed a "regular" and an "irregular" pore network, which differ in their local connectivity. For regular pore networks, the number of neighboring pore bodies connected to a pore body is the same for all pores, i.e., $\overline{N_t} = N_{t,i} = 4$, except at the outer edges of the network. On the contrary, irregular networks have locally varying connectivity, $N_{t,i}$. In this work, irregular networks were generated by modifying a regular network with initially uniform connectivity $N_t = 8$, by randomly removing pore throats until an average connectivity $\overline{N_t} = 4$ was reached. To prevent the occurrence of isolated pore bodies in the network, local pore connectivity was kept to a minimum value of 2. A total of 300 independent realizations of irregular networks were generated, so as to extract parameter values from the simulation results that are statistically representative. Additional parameters of the networks, including physical properties of the N_2–water system considered in this study, are listed in Table 1.

Table 1 Input parameters for the pore-network simulations. [a] Sander (2023), [b](Bell et al. 2014), [c] Cadogan et al. (2014)

Parameter [units]	Symbol	Value
Radius of pore body [μm]	R_p	2.5
Throat length [μm]	L_t	2
Throat radius [μm]	R_t	1.5
Initial saturation of liquid [−]	f^0	1
Initial bubble radius [μm]	R^0	1
Pressure [Pa]	P^0	101,325
Temperature [K]	T	298.15
Henry's constant[a] [mol/Pa/m^3]	k_H	6.4×10^{-6}
Interfacial tension[b] [N/m]	γ	0.0721
Diffusion coefficient[c] [m^2/s]	$\mathcal{D}$	1.93×10^{-9}
Molecular weight [kg/mol]	M	0.028

2.4 Simulation Scenarios With and Without Bubbles

To isolate the effect of bubble dissolution on the evolution of the solute concentration field, we compare the model predictions for two scenarios: a lattice of bubbles undergoing dissolution, and a situation where the same pores contain the same total mass of gas as dissolved solute in place of bubbles. Specifically, the initial lattice occupies 25 pore bodies with coordinates (in p.u.) $-2 \leq x \leq 2$ and $-2 \leq y \leq 2$ (Fig. 2).

At the start of the simulations, $f^0 = f(t = 0) = 1$ throughout the network, i.e., the liquid phase is saturated and its concentration is $C_\mathrm{p}^0 = k_\mathrm{H} M P^0 \equiv \mathrm{C1}$. The simulation is initialized by populating the center of the network with either a lattice of 25 bubbles with uniform size, $R^0 = 1$ μm (simulation with bubbles) or with solute (simulation without bubbles) at a concentration $C_\mathrm{p}^0 = \mathrm{C2}$, such that the total mass of solute is the same as in the simulation with bubbles:

$$\mathrm{C2} = \frac{\mathrm{C1}(V_\mathrm{p} - V_\mathrm{b}^0) + m_\mathrm{b}^0}{V_\mathrm{p}}, \tag{8}$$

where V_p is the volume of the pore body, $V_\mathrm{b}^0 = 4\pi(R^0)^3/3$ is the initial bubble volume, and $m_\mathrm{b}^0 = \rho_\mathrm{b} V_\mathrm{b}^0$ is the initial bubble mass, with ρ_b calculated from Eq. 2 with $R_i = R^0$. Therefore, simulations with bubbles consider both diffusion in the liquid and diffusion through the liquid–gas interface, while simulations without bubbles consider only diffusion in the liquid. The radius of the pore body used in the simulations, $R_\mathrm{p} = 2.5$ μm, ensures that $R_i < R_\mathrm{p}$ is typically satisfied (unless the bubble radius grows significantly) and that during bubble dissolution the more stringent criterion $R_i \ll R_\mathrm{p}$ is also satisfied.

3 Effective Diffusion And Dissolution Properties

3.1 Method of Moments

The method of moments (MoM) is a convenient approach to investigate solute transport in terms of macroscopic averaged quantities, such as the mean or the variance of the solute concentration field, and their temporal evolution (Li et al. 2018). In the following, we present

the definition of the spatial moments considered for this study, while their numerical implementation in pore network coordinates is described in Sect. 3.2.

For a continuous function $g(x, y, t)$ that describes the spatial and temporal distribution of the solute mass in an infinite two-dimensional domain (x, y), the raw (m) and centered (M) moments are defined as follows:

$$m_{lk} = \iint_{-\infty}^{\infty} g(x, y, t) x^l y^k \, dx \, dy, \tag{9a}$$

$$M_{lk} = \iint_{-\infty}^{\infty} g(x, y, t)(x - \mu_x)^l (y - \mu_y)^k \, dx \, dy, \tag{9b}$$

where the subscripts l, k take a value of either 0, 1 or 2, as described in the following. The zeroth moment ($m_{00} = M_{00}$) describes the total mass in the system, which is constant over time for a closed domain, due to mass conservation. Accordingly, the normalized first raw moments describe the coordinates of the distribution's center of mass (μ_x, μ_y):

$$\mu_x = \frac{m_{10}}{M_{00}}, \tag{10a}$$

$$\mu_y = \frac{m_{01}}{M_{00}}. \tag{10b}$$

For Fickian diffusion in a uniform domain, the center of mass is stationary, i.e., $\mu_x(t) - \mu_x(t = 0) = 0$ and $\mu_y(t) - \mu_y(t = 0) = 0$ and the Einstein–Smoluchowski relationship states that the variance of the solute concentration plume is proportional to the diffusion coefficient, $\mathcal{D}$, and grows linearly with time, i.e., $\sigma^2 = 2\mathcal{D}t$. Accordingly, in a two-dimensional domain, elements of the diffusion tensor can be extracted from the first derivative of the corresponding variances with respect to time:

$$\mathcal{D}_x = \frac{1}{2} \frac{d\sigma_{xx}^2}{dt}, \tag{11a}$$

$$\mathcal{D}_y = \frac{1}{2} \frac{d\sigma_{yy}^2}{dt}. \tag{11b}$$

The elements of the distribution's variance tensor are obtained by normalizing the centered second moments, such that:

$$\sigma_{xx}^2 = \frac{M_{20}}{M_{00}}, \tag{12a}$$

$$\sigma_{yy}^2 = \frac{M_{02}}{M_{00}}, \tag{12b}$$

$$\sigma_{xy}^2 = \sigma_{yx}^2 = \frac{M_{11}}{M_{00}}. \tag{12c}$$

For an isotropic medium, such as a regular pore network with constant properties, the variance in $x-$ and $y-$ direction is expected to be the same ($\sigma_{xx}^2 = \sigma_{yy}^2$), meaning that $\mathcal{D}_x = \mathcal{D}_y$.

3.2 Mass Distribution Functions in a Pore Network

Dissolving bubbles are point sources of solute into the surrounding liquid that are distributed throughout the pore network. The characterization of the resultant evolution of solute distribution can shed light on the effects arising from the pore-network geometry on the dissolution

process. To this end, we define below so-called mass distribution functions, which will be used to compute the spatial moments defined in Sect. 3.1.

The total mass of solute at each time step, t, is computed as the sum of mass of solute in the gas (m_b) and liquid phases (m_d) in each pore body $i = 1, \ldots P$:

$$M_\mathrm{tot} = \sum_{i=1}^{P} (m_{\mathrm{b},i}(t) + m_{\mathrm{d},i}(t)) \tag{13}$$

where $m_\mathrm{b} = 4\pi R^3 \rho_\mathrm{b}/3$ and $m_\mathrm{d} = (V_\mathrm{p} - m_\mathrm{b}/\rho_\mathrm{b})C_\mathrm{p}$. We note that R, C_p and ρ_b are time-dependent variables, while M_{00} is a constant due to mass conservation in a closed system. Because the dissolution process introduces additional mass in the liquid phase, we further define the so-called excess dissolved mass:

$$\Delta m_{\mathrm{d},i}(t) = m_{\mathrm{d},i}(t) - m_\mathrm{d}^0 \tag{14}$$

where $m_\mathrm{d}^0 = \mathrm{C1}(V_\mathrm{p} - kV_\mathrm{b}^0)$ is the initial amount of dissolved solute in each pore ($k \in \{0, 1\}$ depending on the absence/presence of a bubble of initial volume V_b^0 in the pore).

The excess dissolved mass is used to obtain the distribution functions g_d and $g_\mathrm{d+b}$ for the calculations of the spatial moments:

$$g_{\mathrm{d},i}(t) = \frac{\Delta m_{\mathrm{d},i}(t)}{\sum_{i=1}^{P} \Delta m_{\mathrm{d},i}(t)} \tag{15a}$$

$$g_{\mathrm{d+b},i}(t) = \frac{\Delta m_i(t)}{\sum_{i=1}^{P} \Delta m_i(t)} \tag{15b}$$

where $\Delta m_i = \Delta m_{\mathrm{d},i} + m_{\mathrm{b},i}$ additionally accounts for solute mass in the gaseous phases. As will be explained below, a distinction between $\Delta m_{\mathrm{d},i}$ and Δm_i is useful when comparing scenarios with bubbles ($\Delta m_{\mathrm{d},i} \neq \Delta m_i$) and without bubbles ($\Delta m_{\mathrm{d},i} = \Delta m_i$), as the effective diffusion coefficient of the network is estimated from $\Delta m_\mathrm{d}, i$, while the center of mass of the lattice is estimated from Δm_i.

The normalization in the definition of the distribution functions implies that at each time $\sum_{i=1}^{P} g_{\mathrm{d+b},i} = \sum_{i=1}^{P} g_{\mathrm{d},i} = 1$. In applying the method of moments (Sect. 3.1), the distribution function $g(x, y, t)$ takes the definition given in Eq. 15a or 15b, and Eqs. 9a and 9b are solved in a finite domain Ω consisting of a rectangular lattice of size $171 \times 171 = P$ pore bodies. At each time step, the numerical evaluation of the integrals is carried out by evaluating and mapping the function g onto the Cartesian $\{x, y\}$ grid of the lattice, and by applying the trapezoidal rule (`trapz` function in MATLAB). As such, the zeroth ($m_{00} = M_{00}$), first (e.g., m_{10}) and second (e.g., M_{20}) moments take units of [p.u.]^2, [p.u.]^3 and [p.u.]^4, respectively. Accordingly, the distribution's center of mass (μ) and variance (σ^2), take units of [p.u.] and [p.u.]^2, respectively.

When applied to the distribution of the excess solute plume, g_d, Eq. 11a and 11b yield effective diffusion coefficients of the pore network, while the estimates obtained upon application of $g_\mathrm{d+b}$ are referred to as the effective dissipation coefficients, to highlight the added contribution of bubble dissolution. To this end, the variance estimated in pore-network units is multiplied by the square of the pore-throat length, which is used to represent the diffusive length across which Fick's law is applied, i.e., $\sigma^2[\mathrm{m}^2] = \sigma^2[\mathrm{p.u.}^2]L_\mathrm{t}^2$. In the absence of bubbles in the network, the coefficient is expected to be constant and smaller than the molecular diffusion coefficient due to the tortuosity of the diffusive pathways.

To investigate the dissolution rate of the bubble lattice, we define the following dimensionless quantity:

$$\psi(t) = \frac{\iint_\Omega \Delta m_{d,i}(t)\, dx\, dy}{\iint_\Omega m^0_{b,i}\, dx\, dy} \tag{16}$$

where m^0_b is the initial mass of solute in the gas phase. By definition, $0 \leq \psi \leq 1$, whereby the upper limit is attained when all bubbles in the lattice have dissolved, i.e., when the amount of excess dissolved solute has reached an amount equal to the initial mass of solute in the gas phase. Because any variation in $\Delta m_{d,i}(t)$ is the direct consequence of bubble dissolution, $d\psi/dt$, quantifies the effective dimensionless dissolution rate of a bubble population.

4 Results

4.1 Dissolution Maps of the Bubble Lattice

Exemplary two-dimensional maps of the solute concentration field at three distinct dimensionless times ($\tau = 2, 5, 10$) are presented in Fig. 3 for simulations conducted with **a** the regular and **b** the irregular pore network. Despite the two networks have the same average connectivity ($N_t = \overline{N_t} = 4$), the evolution of the solute concentration field differs substantially. In the regular network, the solute plume expands radially and uniformly. On the contrary, the solute plume in the irregular network is distorted and shows a certain degree of asymmetry. Notably, the dissolution pattern of the bubble lattice is also remarkably different between the two cases. While in the regular network a fairly uniform dissolution front is observed that propagates inwards, the dissolution in the irregular network is more erratic. For instance, some bubbles on the most outer layer of the original lattice have a longer lifetime than bubbles in the inner layers of the lattice. As a result, the network topology of the bubble lattice also evolves with time, becoming more distorted and sparser. Specifically, we note that the distance between a bubble pair in the irregular network may become greater than an individual pore-throat length.

Figures 3(c) (regular network) and 3(d) (irregular network) show the normalized radius, $z = R/R^0$, of the bubbles as a function of the dimensionless time, τ. For the regular pore network, the behavior of the bubble lattice can be described by six characteristic curves, which are mapped onto specific locations in the network (see color coding and diagram in the inset). In fact, the regularity of the network is such that multiple bubbles follow the exact same $z - \tau$ behavior and dissolve simultaneously. We can observe that bubbles in the corners of the outermost layer have the shortest lifetime. The bubble in the center of the lattice is the last to dissolve and it experiences periods of alternating dissolution and growth, due to local solute concentration development resulting from the dissolution of bubbles in the neighboring layers. This characteristic inward propagation of the dissolution front is the manifestation of the so-called diffusive shielding effect, which has been previously reported for microbubbles dissolution in the bulk (Michelin et al. 2018). In the irregular network, more dissolution patterns are identified (14 distinct characteristic curves) and the regular dissolution pattern of bubbles is no longer observed, as indicated by the inset. For the specific realization of the network plotted in the figure, the last bubble to dissolve is located in the right corner of the second layer. Notably, its lifetime ($\tau \approx 22$) is substantially extended relative to the dissolution time of the same bubble in the regular network ($\tau \approx 12$). Its lifetime is also extended relative to the largest lifetime in the regular network ($\tau \approx 20$). Such delayed dissolution is the direct result of the significant growth (up to $z \approx 1.25$) experienced by the bubble—a feature that is

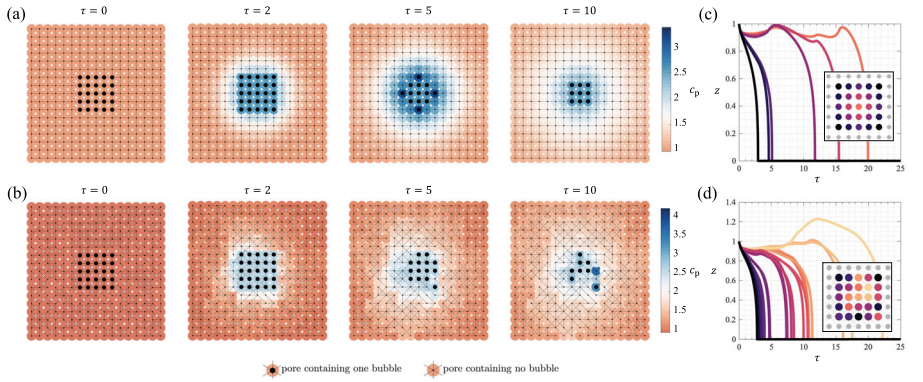

Fig. 3 Collective dissolution of a bubble lattice (25 bubbles with initial radius, $R^0 = 1\ \mu$m) in a regular pore network (top row, connectivity $N_t = 4$) and an irregular pore network (bottom row, average connectivity $\overline{N_t} = 4$). Panels (**a**) and **b** are two-dimensional maps of the solute concentration at three dimensionless times, $\tau = \{0, 2, 5, 10\}$; the configuration at $\tau = 0$ is identical for both pore networks and is not shown. For better visualization, only the center of the pore network is shown ($17 \times 17 = 289$ pores). The color of each pore body indicates a normalized solute concentration, $c_p = C_p/C1$ (initial saturation, $f^0 = 1$) and a black circle indicates the presence of a bubble. Panels (**c**) and **d** show the normalized radius, $z = R/R^0$, of the bubbles as a function of the dimensionless time, τ. The curves are color-coded based on the bubble lifetime, and the corresponding location in the network is shown in the inset

characteristic of irregular networks. On the contrary, shorter periods of growth are observed in the regular network and bubbles never exceed their original size ($z \leq 1$).

4.2 Local Connectivity Effects

As anticipated in the previous section, the irregular connectivity in a pore network alters the dissolution pattern of a bubble cluster relative to that in a network with uniform connectivity. To investigate behaviors dictated by the local connectivity, in this section we present results of simulations with single isolated bubbles. Figure 4 presents the evolution of the normalized radius of the bubble, $z = R/R^0$ (top row), and of the normalized concentration difference, $\Delta c = (C_s - C_p)/|C_s^0 - C1|$ (bottom row), as a function of the dimensionless time, τ, at different levels of initial liquid saturation, $f^0 = 0.6 - 3$. Results obtained on the regular network ($N_t = 4$) are presented with a dotted line, while a solid line is used to represent those obtained on the irregular network ($\overline{N_t} = 4$). In the latter case, three cases are investigated which differ in the local connectivity of the pore body containing the bubble, namely $N_t = 3$ (panels a,d), $N_t = 5$ (panels b,e), and $N_t = 5$ (panels c,f).

Irrespective of the type of network, we observe that the bubble grows for simulations above the so-called threshold saturation, $f_{eq}(R^0 = 1\ \mu\text{m}) = 2.4$, while it dissolves completely when $f^0 < f_{eq}$. As expected, the rate of change of the bubble radius depends on f^0. Specifically, the rate of dissolution increases with time as a result of the increase in Laplace pressure with decreasing radius ($P_b \propto R^{-1}$). As a consequence, the concentration of solute in the pore body increases—outlining a pattern that mirrors the one observed for the bubble radius. While they show a similar behavior to the dissolution curves, the growth curves indicate a much slower evolution in both z and Δc. We also note that for dissolving bubbles, the final dissolution time is always larger than unity ($\tau > 1$); this is expected, as solute transport in the pore network can occur only through pore throats, as opposed to transport

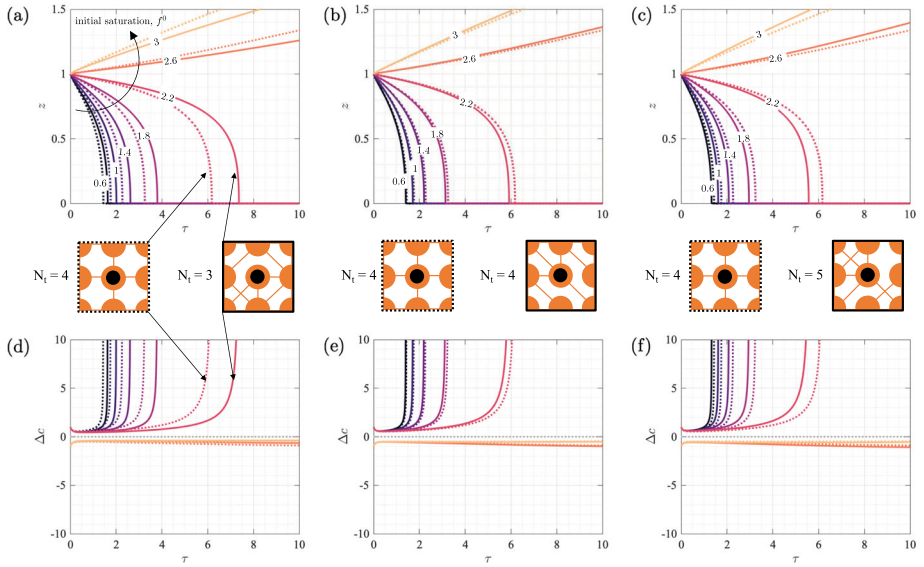

Fig. 4 "Evolution of the dimensionless bubble radius $z = R/R^0$ (top row) and of the normalized concentration difference $\Delta c = (C_s - C_p)/|C_s^0 - C1|$ (bottom row) as a function of the dimensionless time, τ, of a single isolated bubble in a regular (dotted line, $N_t = 4$) and irregular (solid line, $\overline{N}_t = 4$) pore network. Simulations carried out with distinct initial solute concentration, $f^0 = \{0.6, 1, 1.4, 1.8, 2.2, 2.6, 3\}$. For the irregular networks, the simulations differ in the local connectivity of the pore body that includes the bubble (see diagram in the inset of each plot): **a** and **d**: $N_t = 3$, **b** and **e**: $N_t = 4$, **c** and **f**: $N_t = 5$.

in bulk liquid. Accordingly, the dotted- and solid-line differ the least for the simulations shown in panels (b) and (e)—cases where the local connectivity surrounding the bubble in the irregular network equals the connectivity of the regular network. On the contrary, the dissolution and growth rate of the bubble in the irregular network with limited connectivity ($N_t = 3 < 4$) is slower than that in the regular network, whereas the opposite is true when the irregular network possesses augmented connectivity ($N_t = 5 > 4$). While the dependence of bubble lifetime on the local pore body connectivity is not an unexpected result, the differences observed for these three cases indicate that its effect on the evolution of the whole bubble lattice is far from trivial to predict.

4.3 Center of Mass of the Solute Plume

Figure 5 shows the temporal evolution of the first moment in $x-$ (μ_x) and $y-$direction (μ_y), computed for the two distribution functions considered in this study: the excess mass in the liquid phase plus the mass of gas in the bubbles, g_{d+b} (top panel) and the excess mass in the liquid phase, g_d (bottom panel). In each plot, the properties computed for the regular network are plotted as a horizontal solid line, while the shaded region encompasses results obtained for 300 independent realizations of the irregular network, with limits corresponding to the minimum and maximum values of the distribution functions computed at each time step. The first moment describes the center of (excess) solute mass in the given coordinate direction. Its evolution in time can be used to assess the mean velocity of the solute plume. Irrespective of the distribution function considered, both μ_x and μ_y remain stationary at the

location corresponding to the pore-network's center {0,0} for the simulations carried out with the regular network. This is in agreement with the two-dimensional maps presented in Fig. 3, where we observed a uniform dissolution of the bubble lattice and a radial expansion of the solute plume with time. As discussed in our previous work (Joewondo et al. 2022), the presence of bubbles does not perturb the symmetry of the expanding solute plume. On the contrary, for the irregular networks, the location of the center of mass can move of up to one pore unit away from the pore-network's center for the time frame considered here (until complete dissolution of the bubbles). This result indicates that for irregular networks, the topology of the network—characterized here by local differences in the connectivity of pore bodies—impacts the evolution of solute plume's centroid. In the following, we discuss the additional potential impact of the presence of bubbles in the network. When the total excess mass in the system is considered (top panels), the displacement of the center of mass appears as more gradual for a network that initially contains bubbles ($\mu(g_{\mathrm{d+b}})$) as compared to a network that doesn't contain bubbles ($\mu(g_{\mathrm{b}})$). This comparison is somewhat misleading, because bubbles are stationary in the network. In fact, when only the excess dissolved mass is considered (g_{d}, bottom panels), the trends outlined by the simulations with and without bubbles are very similar over the whole duration of the simulations. This result indicates that the presence of bubbles has a negligible impact on the evolution of the solute plume's centroid—also for uniformly irregular networks. This conclusion shall remain valid as long as bubbles are small enough not to interfere with the transport properties of the liquid saturating the pore network. Yet, each network realization produces a distinct curve within the color-shaded regions, resulting in a distinct mean velocity of the solute plume.

4.4 Effective Diffusion and Dissipation Coefficients

We first consider simulations without bubbles with the aim of quantifying the effective diffusion coefficients of both regular and irregular pore networks. To this end, we analyze the evolution of the second spatial moment of the concentration field in both the $x-$ and $y-$directions. The xx element of the variance of the distribution function, g_{d}, is plotted as a function of the dimensionless time, τ, in Fig. 6a. The corresponding results of the yy element are not shown as they are identical to those discussed here. Again, simulations with a regular network are plotted as lines, while those with the irregular networks are represented by the color-shaded region (300 realizations). The limits of the latter correspond to the minimum and maximum values of the distribution function computed at each time step. For the simulations with the regular network, the variance σ^2 grows linearly with time. This is the expected result for a diffusing point source in a uniform domain. While also for the irregular networks σ^2_{xx} and σ^2_{yy} behave identically, their temporal evolution approaches linearity only at late times ($\tau > 15$). Specifically, as indicated by the two solid lines, for $\tau > 15$ the slope on both sides of the shaded region approaches the value observed for the regular network. We refer to this limiting behavior as asymptotic macroscopic diffusion. These gradients, normalized by the factor $2\mathcal{D}$ ($\mathcal{D}$ being the molecular bulk diffusion coefficient), are plotted in Fig. 6b to represent the corresponding effective diffusion coefficient ($\mathcal{D}_x$—see Eq. 11). Simulations using the regular network result in a constant value of the gradient, i.e., $\mathcal{D}_x \approx 0.22\mathcal{D}$, indicating that the tortuosity of the pore network with connectivity $N_{\mathrm{t}} = 4$ yields a 4.5fold decrease in the diffusion coefficient. For the irregular networks, we obtain—on average—-a value of the effective diffusion coefficient at $\tau > 15$ that is similar to the regular network, albeit with variations of approximately $\pm 15\%$ among the different realizations of the network ($\mathcal{D}_x \approx 0.22\mathcal{D} \pm 0.03\mathcal{D}$, corresponding to $d\sigma^2/dt \pm 0.06\mathcal{D}$). At

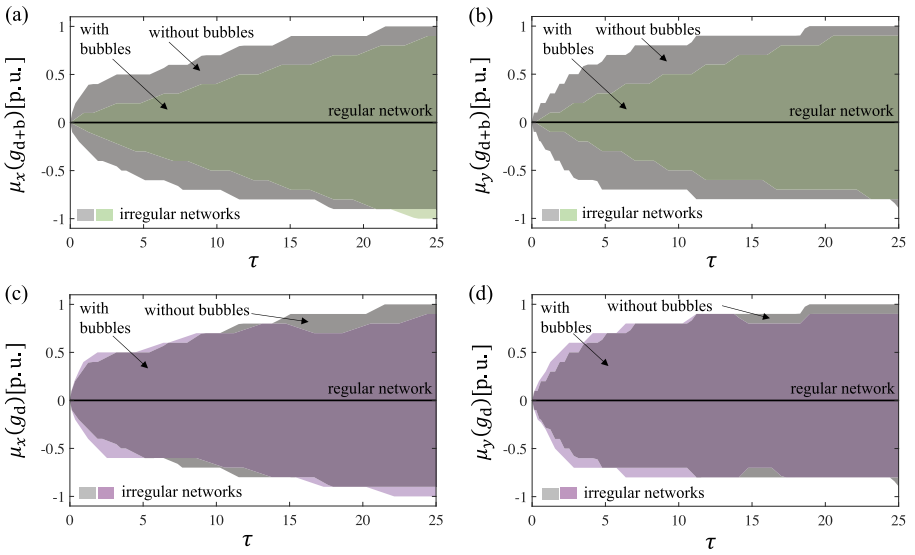

Fig. 5 Temporal evolution of the of the first moments (μ_x - panels **a** and **c**, and μ_y - panels **b** and **d**) of the distribution functions g_{d+b} (total mass, top plots) and g_d (dissolved mass, bottom plots) as a function of the dimensionless time, τ. Results labeled as "with bubbles" are obtained when the network is initialized with a lattice of bubbles and $C_p^0 = C1$. Results labeled as "without bubbles" are obtained when solute of concentration $C_p^0 = C2 > C1$ is used in place of bubbles in the lattice. The location of the spatial moment is expressed in dimensionless pore units. The solid lines represent results of simulations in the regular network (with and without bubbles), while the shaded areas encompass all results for the irregular network (gray represent simulations without bubbles, while magenta (g_d) and green (g_{d+b}) represent simulations with bubbles, respectively, with 300 realizations each)

earlier times ($\tau < 10$), stronger variations in the gradient are observed between different realizations (up to $d\sigma^2/dt \pm 0.15\mathcal{D}$). This result indicates that regular and irregular networks with equivalent average connectivity behave similarly at sufficiently long times (here $\overline{N}_t \approx N_t = 4$). However, variations in the local connectivity of the network results in the asymptotic behavior only being seen after movement through several pore throats, i.e., when the plume occupies an area that is large enough. As indicated by the maps shown in Figure 3, for our simulations this limit is attained for $\tau > 10$, when the radius of the solute plume has reached approximately 8 pore-throat lengths.

We now consider simulations with bubbles, recalling that we will refer here to an effective coefficient of dissipation rather than diffusion. In Fig. 6c, the variance of the distribution functions g_d (black) and g_{d+b} (purple) are plotted as a function of the dimensionless time, τ, for the regular network (solid lines with circles) and irregular networks (shaded areas). For the simulations conducted in the regular network, we observe that both $\sigma^2_{xx}(g_d)$ and $\sigma^2_{xx}(g_{d+b})$ grow in time and approach linearity only at late times ($\tau > 20$). Notably, the variance for the simulations with bubbles is always below the corresponding estimates obtained for the simulations in the regular network without bubbles (dotted line). This observation indicates that the presence of bubbles not only delays the attainment of asymptotic behavior, but also effectively reduces the spatial extent of the solute plume relative to the situation without bubbles present in the network. When comparing the variance computed with the two distribution functions, we note that the variance is further reduced when the mass of solute in the gas phase is accounted for, i.e., $\sigma^2_{xx}(g_{d+b}) \leq \sigma^2_{xx}(g_d)$ for $\tau > 0$. This result is some-

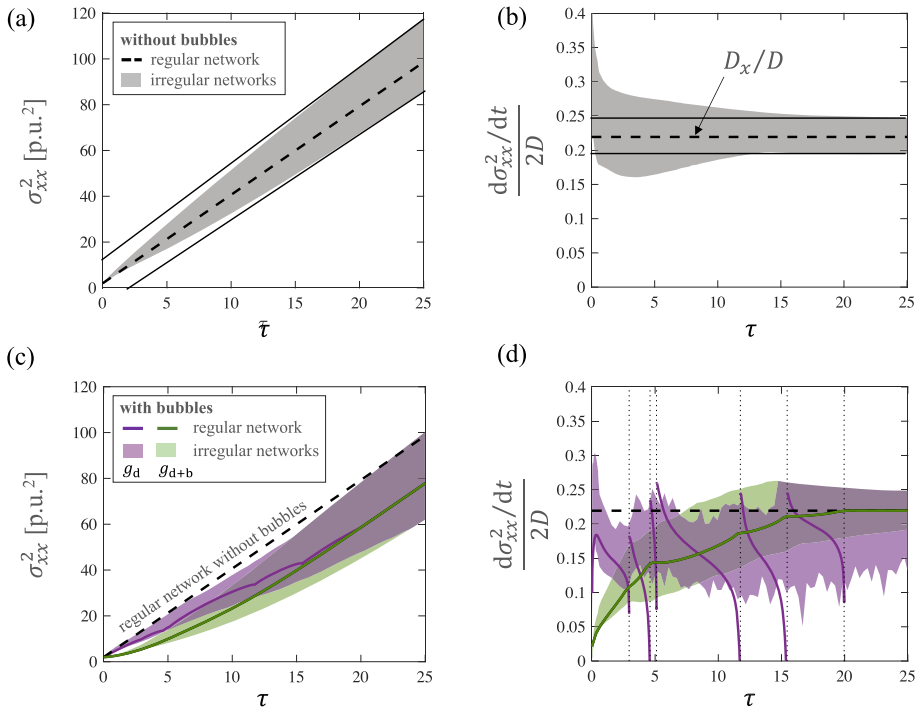

Fig. 6 Temporal evolution of the variance (σ^2) and rate of change of the variance ($d\sigma^2/dt$) of the distribution functions g_d and g_{d+b} in the x-coordinate. Results of simulations without bubbles are shown in panel (**a**) and **b** as a function of the dimensionless time, τ, for the regular network (dotted line) and the irregular networks (shaded area). The corresponding results of simulations with bubbles are shown in panel (**c**) and **d** for the regular network (solid line) and the irregular networks (shaded area), their color depending on whether they represent g_d (magenta) or g_{d+b} (green). The normalization of the rate with the factor $2D$ (see Eqs. 11a and 11b) is used to obtain an estimate of the effective diffusion and dissipation coefficients of the pore network (D_x)

what expected, as bubbles are distributed uniformly in the center of the domain and carry a substantial amount of solute. In fact, upon complete dissolution ($\tau \approx 20$), the curves associated to the two distribution functions converge, because from this time onwards $g_d = g_{d+b}$. Analogous observations can be made for the results obtained with the irregular networks, as indicated by the shaded gray and purple areas. However, as observed for the simulations without bubbles in Fig. 6a, also in this case the results are distributed across a range of values of σ^2_{xx} ($\pm 25\%$ upon attainment of the asymptotic regime at $\tau > 20$).

Figure 6d shows the rate of change of the variance σ^2_{xx} (normalized by $2\mathcal{D}$) as a function of the dimensionless time, τ, for the same simulations discussed above. We observe that when computed using the distribution function g_{d+b}, $d\sigma^2_{xx}/dt$ increases monotonically from a value of approximately $0.04\mathcal{D}$ to the asymptotic value observed for simulations without bubbles, i.e., $D_x \approx 0.22\mathcal{D}$. This behavior conforms with the observations made above that the presence of bubbles slows down the process of solute dissipation compared to diffusive transport driven exclusively by a source of dissolved solute. The results obtained on the irregular networks (purple-shaded area) outline a similar behavior and converge to the solution obtained for networks without bubbles for $\tau > 20$, i.e., when the last bubble in the lattice has dissolved. The picture outlined by the results obtained using the distribution function g_d is more complex.

For the regular network, we observe a discontinuous and strongly non-monotonic behavior of $d\sigma_{xx}^2/dt$ that is largely driven by the sudden dissolution of bubbles. As discussed in Sect. 4.1, in a regular network bubbles at specific locations in the bubble lattice dissolve simultaneously, meaning that there is a sudden release of solute in the corresponding pore bodies. Again, upon completion of the dissolution process ($\tau > 20$) the solution converges to $\mathcal{D}_x \approx 0.22\mathcal{D}$. This discontinuities are also observed in the simulations with the irregular networks (gray-shaded region), albeit these are now less pronounced, because the distribution of dissolution times of individual bubbles is broader. This effect has been discussed in Sect. 4.2 and is to be traced back to local connectivity effects in the network.

4.5 Effective Dissolution Rate of a Bubble Lattice

In Sect. 3.2, the function $\psi(\tau)$ was introduced that describes the cumulative amount of solute that has been transferred from the gas phase to the liquid phase up to a given time τ. When applied to a bubble lattice, its rate of change, $d\psi/d\tau$, can thus be used to estimate the effective rate of dissolution of the bubble lattice. We compare in Fig. 7 the temporal evolution of the function $\psi(\tau)$ (panel a) and $d\psi/d\tau$ (panel b) for an individual bubble (dotted line) and for a bubble lattice (solid line) dissolving in a regular pore network. The comparison of these two cases allows us shedding light on the role of collective effects in affecting the rate of dissolution of a bubble lattice. In fact, when analyzing ψ (or $d\psi/d\tau$) for the case of an individual bubble, we are effectively analyzing a bubble lattice in which each individual bubble behaves unaware of the other bubbles. The results corresponding to analogous situations in the irregular pore networks are represented by the shaded areas surrounding the two curves.

Collective effects substantially reduce the rate of dissolution of bubbles in a bubble lattice. In Fig. 7a, we observe that for the regular network, complete dissolution ($\psi = 1$) is reached at $\tau = 1.9$ and $\tau = 20.3$ for the individual bubble and for the bubble lattice, respectively. For the irregular networks, a similar delay is observed, i.e., $1.6 \leq \tau \leq 4.3$ for the isolated bubble and $14.8 \leq \tau \leq 26$ for the bubble lattice, whereby the reported ranges reflect differences in the

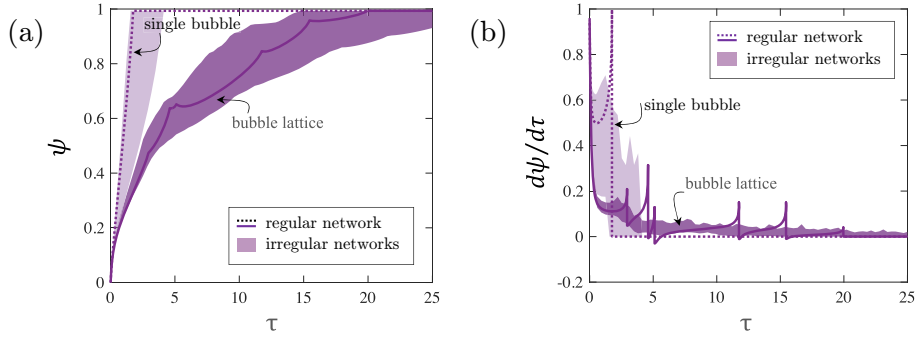

Fig. 7 **a** Normalized cumulative excess mass of dissolved solute, ψ, as a function of the dimensionless time, τ, for a single bubble (dotted line, $R^0 = 1\ \mu$m) and a bubble lattice (solid line, 25 bubbles, all with $R^0 = 1\ \mu$m) dissolving in the regular pore network at initial liquid saturation, $f^0 = 1$. Results for the same cases in the irregular networks (300 independent realizations) are represented by the gray-shaded areas. **b** $\mathrm{d}\psi/\mathrm{d}\tau$ as a function of τ for the same cases presented in (**a**). The vertical dotted lines represent characteristic times at which multiple bubbles in the lattice have completely dissolved (regular pore network)

pore connectivity distribution of each realization of the irregular pore network. Most notably, while the curve of the individual bubble shows the characteristic acceleration associated with the dependence of the Laplace pressure on the bubble radius, the opposite behavior is observed for the bubble lattice. This deceleration is more readily seen in Fig. 7b ($d\psi/d\tau$ vs τ) for the dissolution of the bubble lattice in the regular pore network (solid line). Specifically, the curve shows short instances of acceleration in the dissolution that are associated with the simultaneous disappearance of bubbles in the lattice and that mimic the behavior of the individual bubble (dotted line). Nevertheless, the dissolution rate of the bubble lattice is substantially smaller and its value decreases with time, indicating that collective effects strongly affects the effectively dissolution kinetics of a bubble lattice. Notably, for the case considered here, collective effects appear to be stronger than effects associated with the local pore connectivity distribution in the network, as the observed variation in $d\psi/d\tau$ (shaded area surrounding the solid curve) is small relative to its overall change during the whole dissolution process. In fact, when such collective effects are removed, much stronger variations in the rate of dissolution are observed (single bubble and shaded area around the curve).

5 Conclusions and Outlook

We have investigated numerically the collective dissolution of microbubbles in regular and irregular pore networks of equal average pore connectivity. Uniformly irregular networks were generated from highly connected regular networks through the iterative random removal of pore throats to yield the chosen average pore connectivity. In a regular network, the dissolution pattern of the bubble lattice moves uniformly inwards. On the contrary, the dissolution pattern of the same bubble lattice in the irregular network becomes erratic as a result of the complex interplay between local pore connectivity and diffusive shielding (collective effects). Notably, bubbles in a irregular network can experience significant growth (up to 25% of the initial radius) before undergoing complete dissolution.

Overall, collective effects reduce the rate of dissolution of bubbles in a bubble lattice and appear to be stronger than effects associated with the local pore connectivity distribution in the network. To rationalize quantitatively the coupled dissolution–diffusion process, we computed the first two spatial moments of the solute concentration field. For each individual network, simulations with and without bubbles were conducted, so as to decouple effects arising from inter- (within liquid) and intra-pore diffusion (through liquid–gas interface) on the observed evolution of the solute plume. The presence of bubbles has a negligible impact on the evolution of the solute plume's centroid for both regular and irregular networks. However, the presence of bubbles reduces the spatial extent of the solute plume relative to a bubble-free network (second spatial moment) and delays the attainment of the limit of asymptotic diffusion.

Overall, the results illustrate the rich variety of dissolution behavior of bubbles in a pore network depending on the presence (or absence) of neighboring bubbles and the local pore connectivity. The networks considered in the present study exhibit modest diversity in structural features relevant to fluid transport, limiting the direct extension of our results to any network with irregular topology. We anticipate that the network topology modulates the relationship between solute transport and the growth/dissolution of bubbles. As such, we anticipate that the effects observed for the irregular networks considered in this work may be exacerbated even further for pore networks of practical porous media, which have a greater variance of pore connectivity as well as pore and throat sizes. In addition to mass transfer

by diffusion, an accurate description of these systems may need to consider solute advection between pores as well as local pressure changes in the liquid arising from bubble dissolution or growth.

Author Contributions All authors contributed to the study conception and design. Data collection and analysis were performed by NJ. The first draft of the manuscript was written by NJ and all authors commented on previous versions of the manuscript. All authors read and approved the final manuscript.

Funding N.J. was funded by the Marit Mohn Scholarship at the Department of Chemical Engineering, Imperial College London.

Data Availability The datasets generated during and/or analyzed during the current study are available from the corresponding authors on reasonable request.

Declarations

Conflict of interest The authors declare no conflict of interest.

References

Adam, K.M., Bloomsburg, G.L., Corey, A.T.: Diffusion of trapped gas from porous media. Water Resour. Res. **5**(4), 840–849 (1969)

Bell, I.H., Wronski, J., Quoilin, S., Lemort, V.: Pure and pseudo-pure fluid thermophysical property evaluation and the open-source thermophysical property library coolprop. Ind. Eng. Chem. Res. **53**(6), 2498–2508 (2014)

Blunt, M.J.: Ostwald ripening and gravitational equilibrium: Implications for long-term subsurface gas storage. Phys. Rev. E **106**(4), 045103 (2022)

Cadogan, S.P., Maitland, G.C., Trusler, J.P.M.: Diffusion coefficients of co_2 and n_2 in water at temperatures between 298.15 k and 423.15 k at pressures up to 45 mpa. J. Chem. Eng. Data **59**(2), 519–525 (2014)

Chalendar, J.A.D., Garing, C., Benson, S.M.: Pore-scale modelling of Ostwald ripening. J. Fluid Mech. **835**, 363–392 (2018)

Dentz, M., Le Borgne, T., Englert, A., Bijeljic, B.: Mixing, spreading and reaction in heterogeneous media: A brief review. J. Contam. Hydrol. **120–121**, 1–17 (2011)

Dillard, L.A., Blunt, M.J.: Development of a pore network simulation model to study nonaqueous phase liquid dissolution. Water Resour. Res. **36**(2), 439–454 (2000)

Duncan, P.B., Needham, D.: Test of the Epstein-Plesset model for gas microparticle dissolution in aqueous media: Effect of surface tension and gas undersaturation in solution. Langmuir **20**(7), 2567–2578 (2004)

Epstein, P.S., Plesset, M.S.: On the stability of gas bubbles in liquid-gas solutions. J. Chem. Phys. **18**(11), 1505–1509 (1950)

Fry, V.A., Selker, J.S., Gorelick, S.M.: Experimental investigations for trapping oxygen gas in saturated porous media for in situ bioremediation. Water Resour. Res. **33**(12), 2687–2696 (1997)

Held, R.J., Celia, M.A.: Pore-scale modeling and upscaling of nonaqueous phase liquid mass transfer. Water Resour. Res. **37**(3), 539–549 (2001)

Holocher, J., Peeters, F., Aeschbach-Hertig, W., Kinzelbach, W., Kipfer, R.: Kinetic model of gas bubble dissolution in groundwater and its implications for the dissolved gas composition. Environ. Sci. Technol. **37**(7), 1337–1343 (2003)

Jiménez-Martínez, J., Anna, P.d., Tabuteau, H., Turuban, R., Borgne, T.L., Méheust, Y.: Pore-scale mechanisms for the enhancement of mixing in unsaturated porous media and implications for chemical reactions. Geophys. Res. Lett. **42**(13), 5316–5324 (2015)

Joewondo, N., Garbin, V., Pini, R.: Nonuniform collective dissolution of bubbles in regular pore networks. Transp. Porous Media **141**(3), 649–666 (2022)

Krevor, S., Blunt, M.J., Benson, S.M., Pentland, C.H., Reynolds, C., Al-Menhali, A., Niu, B.: Capillary trapping for geologic carbon dioxide storage - From pore scale physics to field scale implications. Int. J. Greenh. Gas Control. **40**, 221–237 (2015)

Li, M., Qi, T., Bernabé, Y., Zhao, J., Wang, Y., Wang, D., Wang, Z.: Simulation of solute transport through heterogeneous networks: analysis using the method of moments and the statistics of local transport characteristics. Sci. Rep. **8**(1), 3780 (2018)

Li, Y., Garing, C., Benson, S.M.: A continuum-scale representation of ostwald ripening in heterogeneous porous media. J. Fluid Mech. **889**, A14 (2020)

Mehmani, Y., Xu, K.: Capillary equilibration of trapped ganglia in porous media: A pore-network modeling approach. Adv. Water Resour. **166**, 104223 (2022)

Michelin, S., Guérin, E., Lauga, E.: Collective dissolution of microbubbles. Phys. Rev. Fluids **3**(4), 1–35 (2018)

Moghadasi, R., Foroughi, S., Basirat, F., R. McDougall, S., Tatomir, A., Bijeljic, B., Blunt, M.J., Niemi, A.: Pore-scale determination of residual gas remobilization and critical saturation in geological co2 storage: A pore-network modeling approach. Water Resour. Res. 59(6), 2022–033686 (2023)

Patmonoaji, A., Suekane, T.: Investigation of CO_2 dissolution via mass transfer inside a porous medium. Adv. Water Resour. **110**(May), 97–106 (2017)

Powers, S.E., Loureiro, C.O., Abriola, L.M., Weber, W.J., Jr.: Theoretical study of the significance of nonequilibrium dissolution of nonaqueous phase liquids in subsurface systems. Water Resour. Res. **27**(4), 463–477 (1991)

Sadeghi, M.A., Aghighi, M., Barralet, J., Gostick, J.T.: Pore network modeling of reaction-diffusion in hierarchical porous particles: The effects of microstructure. Chem. Eng. J. **330**, 1002–1011 (2017)

Sander, R.: Compilation of henry's law constants (version 5.0.0) for water as solvent. Atmos. Chem. Phys. **23**(19), 10901–12440 (2023)

Schmelzer, J., Schweitzer, F.: Ostwald ripening of bubbles in liquid-gas solutions. J. Non-Equilib. Thermodyn. **12**, 255–270 (1987)

Shen, L., Chen, Z.: Critical review of the impact of tortuosity on diffusion. Chem. Eng. Sci. **62**(14), 3748–3755 (2007)

Turkoz, E., Brandman, J., Ertas, D., Hunter, G.L.: Understanding diffusion-controlled bubble growth in porous media using experiments and simulations. Phys. Rev. E **108**, 015105 (2023)

Wang, C., Mehmani, Y., Xu, K.: Capillary equilibrium of bubbles in porous media. Proc. Natl. Acad. Sci. **118**(17), 2024069118 (2021)

Xu, K., Bonnecaze, R., Balhoff, M.: Egalitarianism among bubbles in porous media: An Ostwald ripening derived anticoarsening phenomenon. Phys. Rev. Lett. 119, 264502 (2017) https://doi.org/10.1103/PhysRevLett.119.264502

Yu, Y., Wang, C., Liu, J., Mao, S., Mehmani, Y., Xu, K.: Bubble coarsening kinetics in porous media. Geophys. Res. Lett. **50**(1), 2022–100757 (2023)